J10.6 **WRF MODELING STUDIES OF LANDFALLING ATMOSPHERIC RIVERS AND OROGRAPHIC PRECIPITATION OVER NORTHERN CALIFORNIA**

Arthur J. Eiserloh, Jr.*, Sen Chiao
San Jose State University, San Jose, California

1. INTRODUCTION

California receives most of its rainfall during its cool season when mid-latitude (ML) cyclones track further south into the northeastern Pacific Ocean. The warm sector within these ML cyclones includes a low-level jet (LLJ) which is responsible for transporting large amounts of heat and moisture from the tropics to the midlatitudes. These relatively thin warm-conveyor belts of heat and moisture transport are known as "atmospheric rivers" (ARs). They are responsible for >90% of the atmosphere's meridional moisture transport at any given time (Zhu and Newell 1998; Ralph et al. 2004). Most ARs affect California during its cool season (October through March) and tap their heat and moisture source directly from the tropics (Neiman et al. 2008a). Ralph et al. (2004) classify ARs as having a narrower width (< 1000 km) relative to their length (> 2000 km) and observed vertically integrated water vapor (IWV) values ≥ 2 cm. About 75% of the horizontal water vapor transport in ARs occurs below 2.25 km., and the LLJs within these ARs rest about 1 km above the ocean surface and usually have a maximum jet strength > 20 ms^{-1} (Ralph et al. 2005).

Previous studies have documented the connection between landfalling ARs and flooding events along the U.S. West Coast (Ralph et al. 2003, 2006; Neiman et al. 2011). Millions of dollars in property damage and fatalities can occur as a result from this type of flood event (Neiman et al. 2002). Although they can occasionally cause flooding, ARs are also responsible for 25-50% of the annual precipitation in the West Coast (Dettinger et al. 2011). Ralph and Dettinger (2012) found that almost all 3-day precipitation events from 1997-2008 that were > 400 mm happened in California, Texas, or the Southeastern U.S. Also, they found that from 1950-2008, > 91% of 3-day precipitation events > 400 mm in the Western U.S. occurred simultaneously with a landfalling AR. Thus, they are a vital water resource and an important connection between California's weather and climate.

Orographically enhanced precipitation is the primary mechanism that causes flooding from landfalling ARs and winter storms along the windward slopes of California's mountain ranges. Because the strength of orographic precipitation is dependent on a variety of variables such as terrain height, upstream moisture content, impinging wind speed, slope steepness, wind direction, etc. (Lin et al. 2001; Neiman et al. 2002; Ralph et al. 2003), mesoscale model short-to-medium range quantitative precipitation forecasting (QPF) for California during high impact AR events can be extremely challenging. With a lack of synoptic vertical profiles over the northeastern Pacific Ocean, data assimilation of asynoptic data is necessary for having the most accurate upstream initial conditions for mesoscale models like the WRF (Weather Research and Forecasting) model.

As a general conclusion for QPF in mountainous regions, Richard et al. (2005) suggested that increased efforts for truly mesoscale assimilation of the initial data for high-resolution numerical weather prediction and more studies on the predictability of convection and precipitation are needed. For landfalling winter storms on the West Coast, WRF has been shown to have a positive moisture bias upstream (Hahn and Mass 2009; Ma et al. 2011) and tends to over predict orographic precipitation (Garvert et al., 2005). Additionally, WRF has been shown to have a wintertime wet bias in both short- and long-term forecasts (Chin et al. 2010). Recently, Ma et al. (2011) assimilated GPS Radio Occultation (RO) soundings from the Constellation Observing System for Meteorology Ionosphere and Climate (COSMIC) satellite mission into WRF using 3-dimensional variational analysis (3DVAR) during a landfalling AR event in the Pacific Northwest and showed that there is a slight improvement in the representation of the moisture profiles, specifically in the lower levels. Although there have been numerous studies on WRF's performance during West Coast winter storms, there are not many WRF data assimilation studies investigating potential ways to improve orographic rainfall forecasting for California during high impact ARs with either (3DVAR) or Four-Dimensional Data Assimilation (FDDA) methods of observation and/or analysis nudging in WRF.

The goal of this study is to advance our understanding of orographic rainfall along the U.S. West Coast. The performance of popular WRF data assimilation methods including 3DVAR, observation nudging, and grid nudging and combinations of them are evaluated on their short-to-medium range precipitation forecasts during a high-impact, multi-day AR event for northern California from 28 November to 3 December 2012. During this event, there were four separate ARs or "episodes" to affect California in less than six days. More attention will be placed on Episode 2 which showed the highest 6- and 12-hourly rainfall rates. The aforementioned data assimilation methods will take advantage of National Oceanic and Atmospheric Administration (NOAA)'s Hydrometeorology Testbed (HMT) surface stations and COSMIC GPS RO vertical profiles for improved initial conditions. Because 3DVAR for WRF has the capability to include COSMIC GPS RO vertical profiles for added

* *Corresponding author address*: Arthur J. Eiserloh, Jr., San Jose State Univ., Dept. of Meteorology and Climate Science, San Jose, CA; email: arthur.eiserloh@gmail.com

moisture observations upstream in the Pacific, we hypothesize that WRF simulations using 3DVAR with COSMIC profiles will produce more reliable representations of the landfalling ARs and more accurate QPFs. In Section 2, the data and methods are outlined. Section 3 depicts the WRF model and experimental design. Section 4 focuses on the synoptic and mesoscale episodes of the AR event. Nested model outcomes with seven numerical experiments are evaluated in Section 5. Conclusions and Remarks are given in Section 6.

2. Data

The surface data network used for this study is NOAA's HMT-West, which originally began in California in the late 1990's from NOAA's field projects CAL-JET and PAC-JET to help improve short-term forecasting of landfalling West Coast winter storms (NOAA 2014). Part of HMT's goal is to allow for research to be conducted on heavy precipitation events that cause flooding and hydrological threats in water basins and river sheds. All available HMT-West California-only surface weather stations (data downloaded from ftp://ftp1.esrl.noaa.gov/psd2/data/) were used for both assimilation purposes and for observation analyses. Not all stations used for this study were equipped with rain gauges. In addition to surface data, available upper air soundings from the National Weather Service (NWS) rawinsonde network were used as well.

In an attempt to improve upstream moisture fields, COSMIC GPS RO soundings were included in some of the assimilation experiments. COSMIC (COSMIC-1/FORMOSAT-3) is a 2006 U.S./Taiwan joint mission that provides ~1500-2000 vertical soundings daily around the globe (Anthes et al. 2008). It consists of 6 low-earth orbiting polar satellites able to indirectly retrieve vertical temperature and moisture profiles of Earth's atmosphere by the atmospheric limb-sounding technique, which acquires vertical profiles of refractivity from radio signals between the satellite itself and a stationary GPS satellite. Through the Abel Transformation, the strength of refractivity is shown to be a function of temperature and vapor pressure (Cucurull et al. 2007). Out of all satellite missions that provide global GPS RO soundings (e.g. CHAMP and GPS/MET), COSMIC was the only one to provide data within our area and time of interest. There are many benefits in using COSMIC GPS RO soundings. They are minimally affected by aerosols and precipitation, they are not affected by instrument drift (Cucurull et al. 2007a), and 90% of the time they are able to get data below 1 km above the surface (Anthes et al. 2008). All soundings were downloaded in the "wetPrf" format from the COSMIC Data Analysis and Archive Center (CDAAC) (cdaac-www.cosmic.ucar.edu/cdaac/index.html). The wetPrf soundings have vertical resolution near 100 m in the lower troposphere (Wick et al. 2008).

An observational analysis and validation of the strength and location of the entire AR event along with the spatial distributions of rainfall accumulations was done with vertical IWV data from the Special Sensor Microwave Imager Sounders (SSMIS) and Stage IV 6-hrly gridded rainfall data from the National Centers for Environmental Prediction (NCEP). The SSMIS data from both the F16 and F17 United States Air Force Defense Meteorology Satellite Program (DMSP) polar orbiting satellites were used. SSMIS is a passively conically scanning microwave radiometer with a ground swath of approximately 1700 km and a grid point size of 25 km (Northrop Grumman 2002). In addition to the disadvantages of polar orbiting satellites (limited areal coverage in the lower latitudes and limited temporal coverage), using the SSMIS water vapor retrieval algorithm has considerable difficulty in areas where heavy rainfall exists (Wentz 1997). In addition to SSMIS, upper-level synoptic height analyses from the North American Regional Reanalysis (NARR) dataset were studied for the AR event.

The NECP Stage IV 6-hrly precipitation data is a regional multi-sensor precipitation analysis or estimate of accumulated rainfall data composed of both observations from rain gauge data and radar derived estimates (Baldwin and Mitchell 1996). The data is quality controlled manually by each NWS River Forecast Center before being gridded onto a 4 km resolution grid. Some inaccuracies in NCEP stage IV data exist in mountainous regions due to lack of rain gauges, radar echo blockage from the mountains, and not enough radar coverage (Jankov et al. 2007).

3. WRF Model Configuration and Experimental Design

3.1. The WRF Model

All simulations for this study were conducted with the Advanced Research WRF (WRF-ARW) model version 3.4 (Skamarock et al. 2008). WRF-ARW is 3-D, non-hydrostatic, fully compressible, and has the terrain-following sigma coordinate system. All experiments were initialized at 0000 UTC 28 November 2012 and run for 138 h until the end of the AR event at 1800 UTC 03 December. All were configured with a two-way nested grid system (Fig. 1) and use the GFS 0.5 degree global analysis and forecasts for initial and boundary conditions. The parent domain has a 12 km horizontal resolution (121 x 121 points) with a nested grid of 3 km horizontal resolution (221 x 273 points). Both domains have a vertical resolution of 51 levels. Because it is configured with an even parent-grid ratio, feedback is turned off. The Thompson graupel (2-moment) microphysics scheme (Thompson et al. 2004) as well as the YSU boundary layer microphysics scheme (Hong et al. 2006) are used. The Thompson scheme was chosen because it has been shown to produce a smaller wet-bias in cold season QPFs over portions of northern California then other popular microphysics scheme options in WRF (Jankov et al. 2007).

3.2. Data Assimilation and Experimental Design

This study uses the two FDDA methods of observation nudging and grid nudging, and 3DVAR, all of which have been available in WRF since 2005 (Liu et al. 2005; Barker et al. 2004) for conducting various experiments that will use either one or a combination of them to test which one gives more accurate QPFs during a high impact AR event for California and also to determine if there is any advantage in combining them. These methods are similar to the methods discussed in Yu et al. (2007). Nudging is an empirical data assimilation method whereas 3DVAR is a statistical method (Huang 2014).

Nudging (i.e. "Newtonian Relaxation") is a FDDA approach that "relaxes" the model's grid toward the observations by introducing artificial variables and weighting terms into the prognostic equations (Stauffer and Seaman 1994). The strength or weight of these artificial terms is determined based on the difference between the observed state and the model state. Stauffer and Seaman (1994) discuss two ways this can be achieved: 1) nudging the model's grid points directly to near-continuous observations that can be spatially and temporally non-uniform (i.e. observation nudging), and 2) nudging the model toward a gridded analysis from synoptic observations which must be time interpolated to match the model's time step (i.e. "grid" nudging).

Observation Nudging can be used for all types of observations but is better for continuous data assimilation of asynoptic observations like surface data, wind profilers, sodars, etc. Observation nudging only uses the observations that are within a user-defined nudging time window. For each model time step that falls within the nudging time window, this method first takes the difference between the model and the observations at each observation location. Next, corrections are made to the model grid points that are within a certain user-defined horizontal radius of influence (RIN_{xy}) from each observation point. These corrections are made via other user-defined nudging factors (G) and both horizontal and vertical weighting functions. Analysis nudging uses the same basic equation setup but does not depend on a RIN for each observation point (See Stauffer and Seaman 1994 for equation specifics). Both forms of nudging are possible for nested domains.

The 3-D variational data assimilation method (3DVAR) is a way to produce the best estimate of the atmospheric state at any given analysis time by iteratively reducing a prescribed quadratic cost-function. Through this iteration, the analysis state that provides the minimum cost function represents the most likely estimate of the analysis solution with the least amount of variance between the observations and the background error from previous model forecasts (Barker et al. 2004). The cost function assumes that the covariances of the background error and observations can be statistically described with Gaussian probability density functions. Three elements are needed for 3DVAR simulations: 1) the background analysis for input into WRFDA; 2) observation datasets (i.e. asynoptic data); and 3) the background error covariance statistical analysis. 3DVAR will incorporate those extra datasets to update the initial conditions for WRF. The time dependent lateral boundary conditions are also updated. 3DVAR can be executed in cold-start mode or cycling mode. For cold-start simulations, 3DVAR takes only the generated background analysis and then assimilated with the model throughout the entire forecast period. The cycling mode is based on the cold-start results (e.g., every 3 hours in this study) as its input background analysis. This cyclic process can continue for as long as it needs.

A total of seven high resolution WRF experiments were performed to evaluate different combinations of nudging and 3DVAR during this high impact AR event (Table 1). The control simulation (CTRL) was conducted without data assimilation. The first four experiments, besides the CTRL run, include FDDA nudging methods and use Cressman-style objective analysis in order to improve the initial and boundary conditions throughout the model integration at 3-h intervals. As shown in Fig. 2, the HMT surface data (p_{sfc},z,t,rh,u,v) or both the HMT surface and sounding data (p,z,t,rh,u,v) are used depending on what data the experiment uses for assimilation purposes. In the second experiment (SN1), only observation nudging was used solely with the HMT surface sites to analyze what the effects of simply surface observation nudging of the HMT surface network had on the QPFs. The HMT surface data is nudged at 3-h intervals throughout the entire forecast period. Although observation nudging is best for real-time almost-continuous data assimilation, a coarser 3-h interval was chosen for SN1 and for all nudging experiments because the nudging is performed over the entire event. All stations have a RIN_{xy} of 40 km with observation nudging coefficients of 3.0 x 10^{-4} s^{-1} for temperature, moisture, and horizontal winds (*t, q, u,* and *v*).

Experiments N2 and N3 combine both observation nudging and grid nudging and include both HMT surface data and upper level sounding data. Grid nudging is included both at the surface and in the upper levels. N2 has a larger RIN_{xy} for all surface and upper air observations of 100 km. Pattantyus (2011) suggested that a larger RIN_{xy} for mesoscale FDDA observation nudging in WRF produces more realistic precipitation patterns in comparison to radar returns in short-term forecasts. N2 has the same observation nudging coefficients as SN1 but with grid nudging coefficients of 6.0 x 10^{-4} s^{-1}. In order to test the effects of different RIN_{xy} values for the upper air soundings and surface data, N3 has an upper air RIN_{xy} of 120 km and a surface RIN_{xy} of 60 km. Both N2 and N3 also have coarse nudging intervals of 3 h.

The last three experiments include COSMIC data and the 3DVAR method but with different data assimilation combinations. Only 46 COSMIC GPS RO soundings were available throughout the event and within the coarse domain. The scattered spatial distribution of RO soundings is shown in Fig. 3a. The 3DVT1 experiment is a hybrid of all three data assimilation techniques (observation nudging, grid nudging, and 3DVAR), and it includes all data sources

(HMT surface, upper air soundings, and COSMIC data). Also, it has the same setting as N3 but does a 3DVAR cold-start at the model start time with a relatively large 12-h time window to take advantage of as many COSMIC soundings as possible. 3DVT2 is purely a cold-start 3DVAR run with the same 12-h time window as 3DVT1 but without nudging. 3DVT3 is a 3DVAR cycling run with both a cycling interval and observation time window of 3 h. Notice that not every 3-h window has COSMIC soundings available, and there is only an average of one sounding per 3-h time window (Fig. 3b).

4. Synoptic and Mesoscale Overview

From 0000 UTC 28 November to 1800 UTC 03 December 2012, four AR episodes made landfall over northern and central California. A deep longwave trough was present over the northeastern Pacific Ocean upstream of an amplified ridge from the Pacific Northwest to Alaska. This blocking event persisted and allowed the upper air pattern to become quasi-stationary. Multiple shortwave troughs circulated around the longwave trough and brought the four AR episodes of high IWV content and heavy precipitation to California within six days (Fig. 4a-d). All episodes except Episode 3 show stronger, more well-defined ARs with IWV values ≥ 30 mm and maximum IWV values possible exceeding 40 mm. Heavy rainfall within the frontal bands prevent SSMIS from getting IWV retrievals in the core of the ARs. The moisture source during Episode 1 originated more directly from the tropics, whereas for the others it was more subtropical in nature and made landfall with a more perpendicular orientation with respect to the coast.

Figure 5 shows the entire event rainfall accumulations from NCEP Stage IV rainfall analysis. This event brought strong orographic precipitation to most of northern California. The three regions that experienced the highest orographic rainfall totals were the Coastal Range, northern Sierra Nevada, and the Trinity Alps/Mount Shasta region. The event maximum of 588 mm (~23.15 in) occurred in Humboldt County, located in the northern Coastal Range. In order to identify when and where the heaviest rainfall rates occurred, every 6- and 12-h interval in the NCEP stage IV data was studied to find the time period and episode that received the highest 6- and 12-hrly accumulations. Table 2 shows the largest 6- and 12- hrly accumulations for all four episodes along with their time periods. Both Episodes 2 and 4 had the largest 6- and 12-hrly accumulations overall with Episode 2 showing slightly higher 6-hrly and 12-hrly rainfall rates of 131 mm (1200—1800 UTC 30th) and 195 mm (1200 UTC 30th—0000 UTC 1st), respectively along the windward slopes of the Santa Lucia Mountain Range near Big Sur (Fig. 6). Although Episode 4 caused more widespread heavy rainfall across most of northern California, it did not produce the largest localized maximum 6-hrly and 12-hrly rainfall rates. Therefore, the focus of the WRF experiments will be evaluated during Episode 2's period of highest 6-hrly rainfall rate within domain 2 (i.e., forecast hours 60-66).

5. Experiment Results

5.1. Characteristics of AR Episode 2

To evaluate the performance of the WRF experiments during Episode 2's maximum 6-hrly rain rate time period (1200—1800 UTC 30 Nov), the experiments' results of accumulated rainfall during this 6-hr period was compared to NCEP Stage IV observations (Fig. 7a). All WRF experiments could not capture the correct location and timing of the front associated with the AR 66 hours into the forecast (Figs. 7b-h). The experiments are much slower to progress the cold front associated with the AR southward. The simulations are not able to correctly predict the localized rainfall maximum in the coastal windward slopes of the Santa Lucia Mountains, and they underestimate the rainfall by almost 60 mm (not shown). Also, the experiments largely overestimate the rainfall behind the front in the northern Coastal Range, Trinity Alps, and Mount Shasta regions. In addition, a large wet bias exists in the Sacramento Valley. With respect to frontal position, all experiments with grid-nudging (N2,N3, and 3DVT1) depict a more N-S orientation of the front in the Sacramento Valley, whereas the ones without grid nudging (CTRL, SN1, 3DVT2, and 3DVT3) show a frontal angle that matches more closely to NCEP stage IV.

In addition to looking at accumulated precipitation during Episode 2, the experiments' representations of the AR in terms of IWV values were compared to SSMIS observations (Fig. 8). At 1623 UTC, SSMIS IWV observations show the landfalling AR with core IWV values between 37-40 mm. Nevertheless, the WRF experiments show the AR lagging behind at the San Francisco Peninsula by a few hours with a less-perpendicular orientation than observations. Although SSMIS cannot attain measurements near the coast, inland, or in heavy rainfall, it can be inferred, as shown in Fig. 8, that the observations show higher IWV values closer to the coast then the WRF experiments. Because the experiments depict the AR as having weaker IWV values closer to the coast and a less perpendicular angle upon landfall, this may be a reason why WRF could not accurately predict the maximum rainfall amount in the Santa Lucia Mountains during Episode 2. Only subtle differences in the landfalling AR exist between each experiment. However, two notable differences stand out. The models with grid-nudging show weaker IWV values but have a larger AR width (Figs 8d-f). Models without grid-nudging show thinner core AR values but with more accurate maximum IWV values (Figs. 8b-c and 8g-h).

Because only minor differences existed in the 2-D fields of rainfall and IWV between the WRF data assimilation experiments, further analyses into the onshore and inland moisture flow, dynamics, and timing of the AR within Episode 2 were carried out in the vertical dimension. A N-S cross section along the California coast, and a W-E cross section across the Sacramento Valley are constructed within domain 2

(Fig. 9). Both cross sections were taken in the middle of the time period at forecast hour 63 (1500 UTC 30 Nov). Figure 10 shows the N-S cross section (line1 in Fig. 9) of relative humidity and wind speed for all experiments. All experiments show a frontal inversion with an upper-level jet around 60 m s^{-1} and a lower-level jet on the warm side with wind speeds around 30 m s^{-1} between 3 and 4 km above the surface. The most notable difference is the substantial smoothing of the results in the grid-nudging experiments (Figs. 10c-e). The non-grid-nudging experiments show more detailed differences especially behind the frontal inversion on the north side (Figs. 10a-b and 10f-g). They demonstrate convective cells and more convective instability behind the cold front. Additionally, the non-grid-nudging models show winds about 5 m s^{-1} stronger near the 3-4 km level in the low-level jet than the models with grid-nudging. Although the models without grid-nudging show the front to be slightly further south, no real dramatic differences in the latitudinal position of the surface front over the ocean are seen. The smoothed-out convective details behind the front and the slightly weaker winds in the low-level jet seen in the grid-nudging model results are most likely caused by nudging the finer scale model grid-points in domain 2 toward the coarser objective analysis grids. Stauffer and Seaman (1994) suggested that assimilating relatively coarse-resolution gridded data onto a finer-scale grid does more harm than good by preventing the model's innate ability to develop finer-scale details.

However, longitudinal and timing differences in the frontal positions between all experiments can be seen more clearly in the W-E cross section (Fig. 11) in the Sacramento Valley. At this time, grid-nudging models are slower to bring the front across the valley than the non-grid-nudging models and still have the cold front moving through the Coastal Range. Here the non-grid-nudging models show a tighter gradient of the southerly wind isotachs, indicating a stronger wind-shift. Of the non-grid-nudging models, the SN1 experiment is the most progressive in its movement of the front. Because all experiments show a slower progression of the actual front and SN1 is the quickest to move the front across the valley, SN1 is also the most accurate of the models in terms of timing and location. Besides, SN1 and 3DVT3 show more evidence of a post-frontal coastal barrier jet forming with higher near-surface southerly wind speeds in the Pacific Ocean west of the coast. Lastly, non-grid-nudging models show a stronger connection of the pre-frontal southerly winds in the lower-levels to the winds in the upper-level jet above 5 km.

5.2. Statistical Comparison of Precipitation over Coastal Ranges and Sierra Nevada

Effects of the various WRF data assimilation methods on rainfall amounts can be seen in different mountainous regions of California as well. For this, two clusters or regions of HMT surface stations were separated in the North Central Coastal Range and in the windward Sierra Nevada, respectively (Fig. 12). For each region, all of the accumulated rainfall time evolutions for each station were averaged to get a site-averaged accumulated rainfall time series for both the observations and the experiments. Locations of the HMT surface sites were interpolated in the WRF experiments in order to get the accumulated rainfall time series. Only HMT stations with good rainfall data were used. There were a total of 8 and 13 stations in the North Central Coastal Range Region and the Windward Sierra Nevada region, respectively. Figure 13 shows the site-averaged accumulated rainfall time evolutions for each of the regions throughout the forecast period. For the North Central Coastal Range region (Fig. 13a), all the WRF experiments on average underestimate the rainfall amounts for the first half of the event. During Episode 2 and near forecast hour 60, the non-grid-nudging models and grid-nudging models diverge in their results. The non-grid-nudging models overestimate the rainfall and the grid-nudging models stay near the observations until the end where they underestimate the rainfall. For the Windward Sierra Nevada region, all the experiments underestimate the rainfall even more until Episode 4 when the non-grid-nudging models recover in the end except for the grid-nudging models that end the event with an underestimation. Similarly, as in the North Central Coastal Range region, the grid-nudging and non-grid-nudging models begin to diverge during Episode 2 two-and-a-half days into the forecast. Additionally, the mean absolute error (MAE) was calculated for each region and for each model (Table 3). For the North Central Coastal Range sites, 3DVT3 had the least MAE, and for the Windward Sierra Nevada sites, 3DVT2 had the least MAE. At the end of the event, SN1 on average best predicted the entire event accumulated rainfall for the North Central Coastal Range sites with the least error. 3DVT3 on average best predicted the entire event accumulated rainfall for the Windward Sierra Nevada sites with the least error.

6. Conclusions and Remarks

Various WRF data assimilation methods of observation nudging, grid nudging, and 3DVAR were evaluated with combinations of data from the HMT surface stations, NWS network soundings, and COSMIC satellite GPS RO soundings during the high impact, multi-day AR event for Northern California from 0000 UTC 28 November to 1800 UTC 03 December 2012 to study how orographic precipitation forecasts during AR events can be improved. During this event, a total of four ARs impacted California within six days producing heavy orographic rainfall and flash flooding. Particularly the second AR episode produced the highest 6- and 12-hrly rainfall rates along the windward slopes of the Santa Lucia Mountains along the coast based on NCEP Stage IV rainfall analysis. The numerical experiments, therefore, focused on the precipitation forecasts during this episode. A total of seven high resolution WRF experiments were designed that employed various WRF data assimilation combinations of observation nudging, grid nudging, and 3DVAR.

Results of the experiments during Episode 2 show that all WRF experiments are a few hours slower than observations with the location and timing of the AR and its associated cold front 66 hours into the forecast. Also, the experiments cannot recapture the maximum 6-hrly rainfall rate in the Santa Lucia Mountains during Episode 2 and largely under predict this amount. It appears that this under-prediction of rainfall was associated with the strength and size of the AR simulated by the models. The non-grid-nudging experiments were the only ones to show IWV values slightly closer to the SSMIS observations but they still underestimated the width, strength, and angle of the landfalling AR. Another reason for the under-prediction of rainfall at the coast could be that a 3 km fine grid resolution may still not be able to resolve cloud microphysics on the steep windward slopes of the Coastal Range. Cross-sections along the coast and across the Sacramento Valley during Episode 2 reveal that grid-nudging the smaller domain to a coarser domain may not be ideal for mesoscale precipitation forecasts because it smooths out some mesoscale features which can affect the rainfall forecast amounts. The cross sections also show that the surface nudging slightly improved the timing of the front.

Overall, the data assimilation experiments without grid-nudging showed the best results in terms of the precipitation forecast time evolution, especially 3DVAR. For the entire event rainfall accumulation time series, the 3DVAR cycling run had the least MAE for the North Coastal Range HMT sites, and the 3DVAR cold start showed the least MAE for the Windward Sierra Nevada sites. The assimilation of the COSMIC soundings appears to be beneficial for precipitation forecasts here especially for the North Central Coastal Range HMT sites. In terms of the precipitation forecasts at the end of the event, the surface observation nudging and the 3DVAR cycling run gave the least error for the North Central Coastal Range Region and the Windward Sierra Nevada region, respectively. It appears observation nudging the surface data only at 3-hr intervals and performing 3DVAR only at 3-hr cycles is not sufficient in short-term forecasts, and only shows promise after forecast hour 60. Future FDDA nudging experiments should be examined without grid nudging, and they should begin with a 6-12 hour nudging pre-forecast initialization period with a finer nudging time-step interval being that FDDA observation nudging is more useful for streams of continuous observations. Lastly, the effect of different initial conditions should be tested for this event as well, as the timing errors appear to be dependent upon the model choice for initial conditions.

Acknowledgements

We thank Timothy Coleman from NOAA/ESRL for assistance with the HMT dataset, Cindy Bruyere from UCAR in assistance with the WRF data assimilation methods, and the other suppliers of the data used. The research was supported by the Grant W911NF-09-1-0441 from the US Army Research Office.

References

Anthes, R.A., and Coauthors, 2008: The COSMIC/FORMOSAT-3 mission: early results. *Bull. Amer. Meteor. Soc.*, **89**, 313–333. doi:10.1175/BAMS-89-3-313.

Baldwin, M.E., and K.E. Mitchell, 1996: The NCEP hourly multisensory U.S. precipitation analysis. *11th Conf. on Numerical Weather Prediction*, Norfolk, VA, Amer. Meteor. Soc., J95-J96.

Barker, D. M., W. Huang, Y.-R. Guo, A. J. Bourgeois, and Q. N. Xiao, 2004: A three-dimensional variational data assimilation system for MM5: implementation and initial results. *Mon. Wea. Rev.*, **132**, 897–914. doi: 10.1175/1520-0493(2004)132<0897:ATVDAS>2.0.CO;2.

Chin, H.-N. S., P. M. Caldwell, and D. C. Bader, 2010: Preliminary study of California wintertime model wet bias. *Mon. Wea. Rev*., **138**, 3556–3571. doi:10.1175/2010MWR3409.1.

Cucurull, L., J.C. Derber, R. Treadon, and R. J. Purser, 2007: Assimilation of Global Positioning System Radio Occultation Observations into NCEP's Global Data Assimilation System. *Mon. Wea. Rev.*, **135**, 3174–3193. doi: 10.1175/MWR3461.1.

Dettinger, M. D., 2011: Climate change, atmospheric rivers, and floods in California—A multimodel analysis of storm frequency and magnitude changes. *J. Amer. Water Resour. Assoc.,* **47**, 514–523.

Garvert, M. F., B. A. Colle, and C. F. Mass, 2005: The 13–14 December 2001 IMPROVE-2 event. part I: synoptic and mesoscale evolution and comparison with a mesoscale model simulation. *J. Atmos. Sci.*, **62**, 3474–3492. doi: 10.1175/JAS3549.1.

Hahn, R. S., and C. F. Mass, 2009: The impact of positive-definite moisture advection and low-level moisture flux bias over orography. *Mon. Wea. Rev*., **137**, 3055–3071. doi: 10.1175/2009MWR2873.1.

Hong, S., Y. Noh, and J. Dudhia, 2006: A new vertical diffusion package with an explicit treatment of entrainment Processes. *Mon. Wea. Rev.*, **134**, 2318–2341. doi:10.1175/MWR3199.1.

Huang, H. 2014: Introduction to WRFDA. WRF Tutorial, NCAR, Boulder, Colorado, January, 2014. [Available online at http://www.mmm.ucar.edu/wrf/users/tutorial/201401/WRFDA_Intro.pdf].

Jankov, I., P. J. Schultz, C. J. Anderson, and S. E. Koch, 2007: The impact of different physical parameterizations and their interactions on cold season QPF in the American River Basin. *J. Hydrometeor*, **8**, 1141–1151. doi: 10.1175/JHM630.1.

Lin, Y.-L., S. Chiao, T.-A. Wang, M. L. Kaplan, and R. P. Weglarz, 2001: Some common ingredients for heavy orographic rainfall. *Wea. Forecasting*, **16**, 633–660. doi:10.1175/1520-0434(2001)016<0633:SCIFHO>2.0.CO;2.

Liu, Y., and co-authors, 2005: Implementation of observation-nudging based FDDA into WRF for supporting ATEC test operations. 2005 WRF Users Workshop, Boulder, Colorado, June, 2005.

Ma, Z., Y.-H. Kuo, F. M. Ralph, P. J. Neiman, G. A. Wick, E. Sukovich, and B. Wang, 2011: Assimilation of GPS radio occultation data for an intense atmospheric river with the NCEP Regional GSI System. *Mon. Wea. Rev*., **139**, 2170–2183. doi:10.1175/2011MWR3342.1.

Neiman, P. J., F. M. Ralph, A. B. White, D. E. Kingsmill, and P. G. Persson, 2002: The statistical relationship between upslope flow and rainfall in California's coastal mountains: observations during CALJET. *Mon. Wea. Rev.*, **130**, 1468–1492. doi:10.1175/1520-0493(2002)130<1468:TSRBUF>2.0.CO;2.

———, F. M. Ralph, G. A. Wick, J. D. Lundquist, and M. D. Dettinger, 2008: Meteorological characteristics and overland precipitation impacts of atmospheric rivers affecting the West Coast of North America based on eight years of SSM/I satellite observations. *J. Hydrometeor.,* **9**, 22–47. doi:10.1175/2007JHM855.1.

———, L. J. Schick, F. M. Ralph, M. Hughes, and G. A. Wick, 2011: Flooding in western Washington: The connection to atmospheric rivers. *J. Hydrometeor.,* **12**, 1337–1358, doi:10.1175/2011JHM1358.1.

NOAA, cited 2014: NOAA’s Hydrometeorology Testbed: Overview. [Available online at hmt.noaa.gov/about/].

Northrop Grumman, 2002: Algorithm and data user manual (ADUM) for the Special Sensor Microwave Imager/Sounder (SSMIS). Tech. Rep., 1-65 pp.

Pattantyus, A. 2011: Optimizing strategies for an observation-nudging-based four-dimensional data assimilation forecast approach with WRF-ARW. *Science and Engineering Apprenticeship Program*, Adelphi, Maryland.

Ralph, F. M., and M. D. Dettinger, 2012: Historical and national perspectives on extreme west coast precipitation associated with atmospheric rivers during December 2010. *Bull. Amer. Meteor. Soc*., **93**, 783–790. doi: 10.1175/BAMS-D-11-00188.1.

———, and Coauthors, 2003: The impact of a prominent rain shadow on flooding in California’s Santa Cruz Mountains: A CALJET case study and sensitivity to the ENSO cycle. *J. Hydrometeor*., **4**, 1243–1264. doi: 10.1175/1525-7541(2003)004<1243:TIOAPR>2.0.CO;2.

———, P. J. Neiman, and G. A. Wick, 2004: Satellite and CALJET aircraft observations of atmospheric rivers over the eastern North-Pacific Ocean during the El Niño winter of 1997/98. *Mon. Wea. Rev*., **132**, 1721–1745. doi: 10.1175/1520-0493(2004)132<1721:SACAOO>2.0.CO;2.

———, ———, and R. Rotunno, 2005: Dropsonde observations in low-level jets over the northeastern Pacific Ocean from CALJET-1998 and PACJET-2001: Mean vertical-profile and atmospheric-river characteristics. *Mon. Wea. Rev.*, **133**, 889–910. doi:10.1175/MWR2896.1.

———, E. Sukovich, D. Reynolds, M. D. Dettinger, S. Weagle, W. Clark, and P. J. Neiman, 2010: Assessment of extreme quantitative precipitation forecasts and development of regional extreme event thresholds using data from HMT-2006 and COOP observers. *J. Hydrometeor*., **11**, 1288–1306. doi: 10.1175/2010JHM1232.1.

Richard, E. and Coauthors, 2005: Quantative precipitation forecasting in mountains regions — pushed ahead by MAP. *Croat. Meteorol. J*., **40**, 65–69.

Skamarock, W.C., and Coauthors, 2008: A description of the Advanced Research WRF version 3. NCAR Tech Note NCAR/TN-475+STR, 113 pp. [Available online at www.mmm.ucar.edu/wrf/users/docs/arw_v3.pdf.].

Stauffer, D. R., and N. L. Seaman, 1994: Multiscale four-dimensional data assimilation. *J. Appl. Meteor.*, **33**, 416–434. doi:10.1175/1520-0450(1994)033<0416:MFDDA>2.0.CO;2.

Thompson, G., R. M. Rasmussen, and K. Manning, 2004: Explicit forecasts of winter precipitation using an improved bulk microphysics scheme. part I: description and sensitivity analysis. *Mon. Wea. Rev.*, **132**, 519–542. doi:10.1175/1520-0493(2004)132<0519:EFOWPU>2.0.CO;2.

Wentz, F. J., 1997: A well-calibrated ocean algorithm for Special Sensor Microwave/Imager, *J. Geophys. Res*., **102**, 8703–8718.

Yu, W., Y. Liu, and T. Warner, 2007: An evaluation of 3DVAR, nudging-based FDDA, and a hybrid scheme for summer convection forecasts using the WRF-ARW model. *18th Conf. on Numerical Weather Prediction*, 25-29 June 2007, Park City, Utah. P2.8.

Zhu, Y., and R. E. Newell, 1998: A proposed algorithm for moisture fluxes from atmospheric rivers. *Mon. Wea. Rev.,* **126**, 725–735. doi:10.1175/1520-0493(1998)126<0725:APAFMF>2.0.CO;2.

Tables and Figures

Table 1: WRF Experimental Designs

Experiments	DA Method(s)	Data Used	DA Specifics
CTRL	none	--------	--------
SN1	observation nudging	HMT surface	RIN_{xy} = 40 km $G_{obs\text{-}nudging}$ = 6.0 x 10^{-4} s^{-1} nudging time interval = 3 h
N2	observation & grid nudging	HMT surface + RAOB	RIN_{xy} = 100 km $G_{grid\text{-}nudging}$ = 6.0 x 10^{-4} s^{-1} Nudging time interval = 3 h
N3	observation & grid nudging	same as N2	Same as N2 except: surface RIN_{xy} = 120 km upper air RIN_{xy} = 60 km
3DVT1	3DVAR cold-start + observation & grid nudging	HMT surface + RAOB + COSMIC GPSRO	3DVAR: t_0 window = 12 h Nudging: same as N3
3DVT2	3DVAR cold-start	same as 3DVT1	t_0 window =12 h
3DVT3	3DVAR cycling	same as 3DVT1	cycling window = 3 h

Table 2: Maximum 6- and 12-hrly Rainfall Rates for Each AR Episode

Episode	Landfall Time Period	Largest NCEP Stg. IV 6-hrly Rainfall Rates		Largest NCEP Stg IV 12-hrly Rainfall Rates	
		Ending Time	**6-hrly Rate**	**Ending Time**	**12-hrly Rate**
1	1200 UTC 28th - 0000 UTC 29th	1800 UTC 28th	62 mm $(6\ h)^{-1}$	0000 UTC 29th	77 mm $(12\ h)^{-1}$
2	1200 UTC 29th - 0600 UTC 1st	1800 UTC 30th	131 mm $(6\ h)^{-1}$	0000 UTC 1st	195 mm $(12\ h)^{-1}$
3	1200 UTC 1st - 0000 UTC 2nd	1800 UTC 1st	104 mm $(6\ h)^{-1}$	0000 UTC 2nd	114 mm $(12\ h)^{-1}$
4	0000 UTC 2nd - 0600 UTC 3rd	1200 UTC 2nd	110 mm $(6\ h)^{-1}$	1800 UTC 2nd	190 mm $(12\ h)^{-1}$

Table 3: HMT site-average mean absolute error

	mean absolute error						
	CTRL	**SN1**	**N2**	**N3**	**3DVT1**	**3DVT2**	**3DVT3**
North Central Coastal Range	13.07	11.52	12.12	11.51	14.63	13.44	10.95
Windward Sierra Nevada	24.09	24.36	39.89	40.15	41.08	22.72	23.40

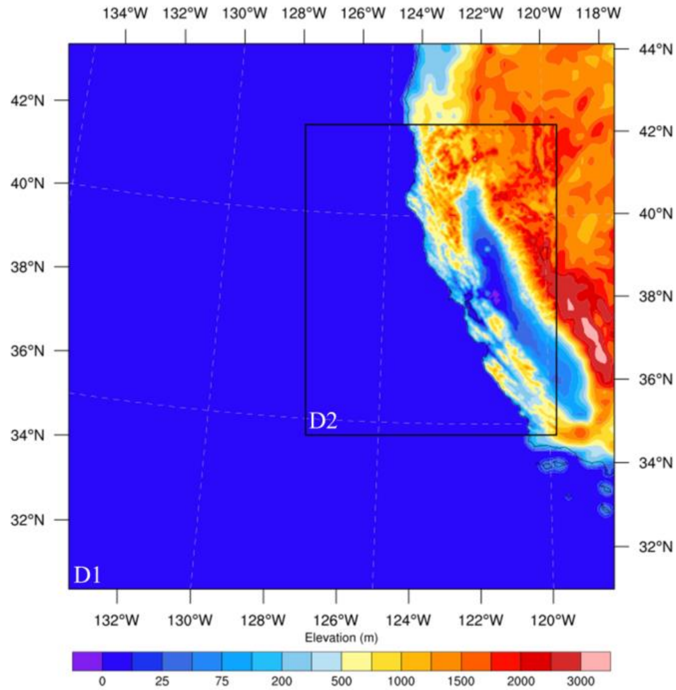

Figure 1: Two-way nested domain used for the WRF experiments.

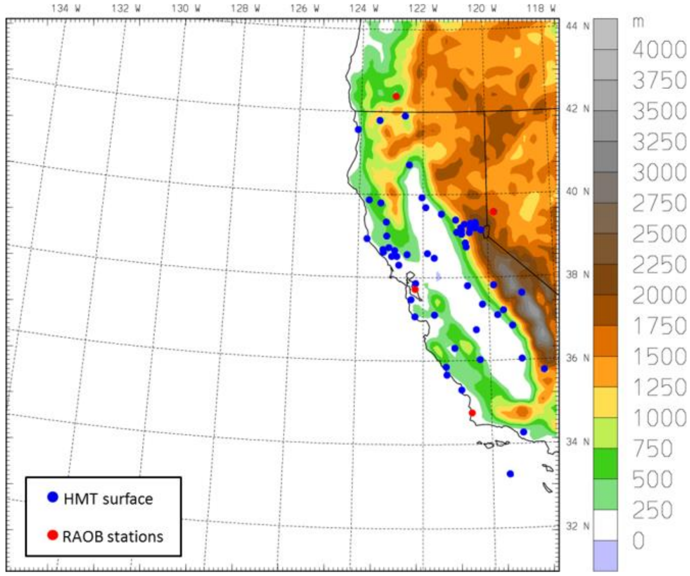

Figure 2: Spatial distribution of the HMT surface stations (blue) and the upper air stations (red) inside parent domain.

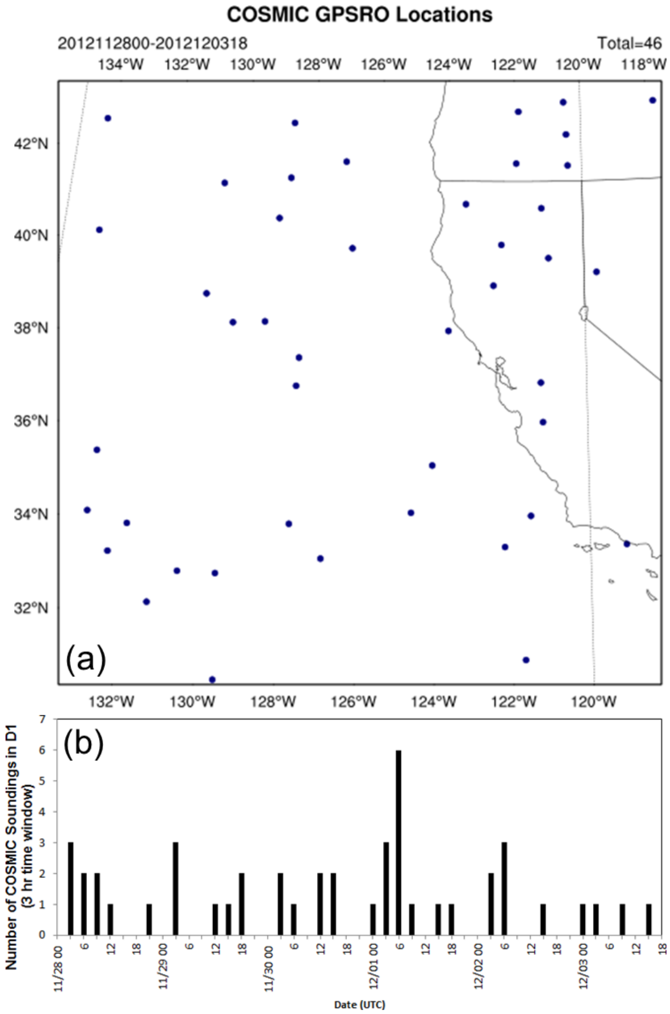

Figure 3: (a) Locations of COSMIC GPS RO soundings from 0000 UTC 28 Nov to 1800 UTC 03 Dec 2012 and (b) the amount of COSMIC soundings for every 3-h time window.

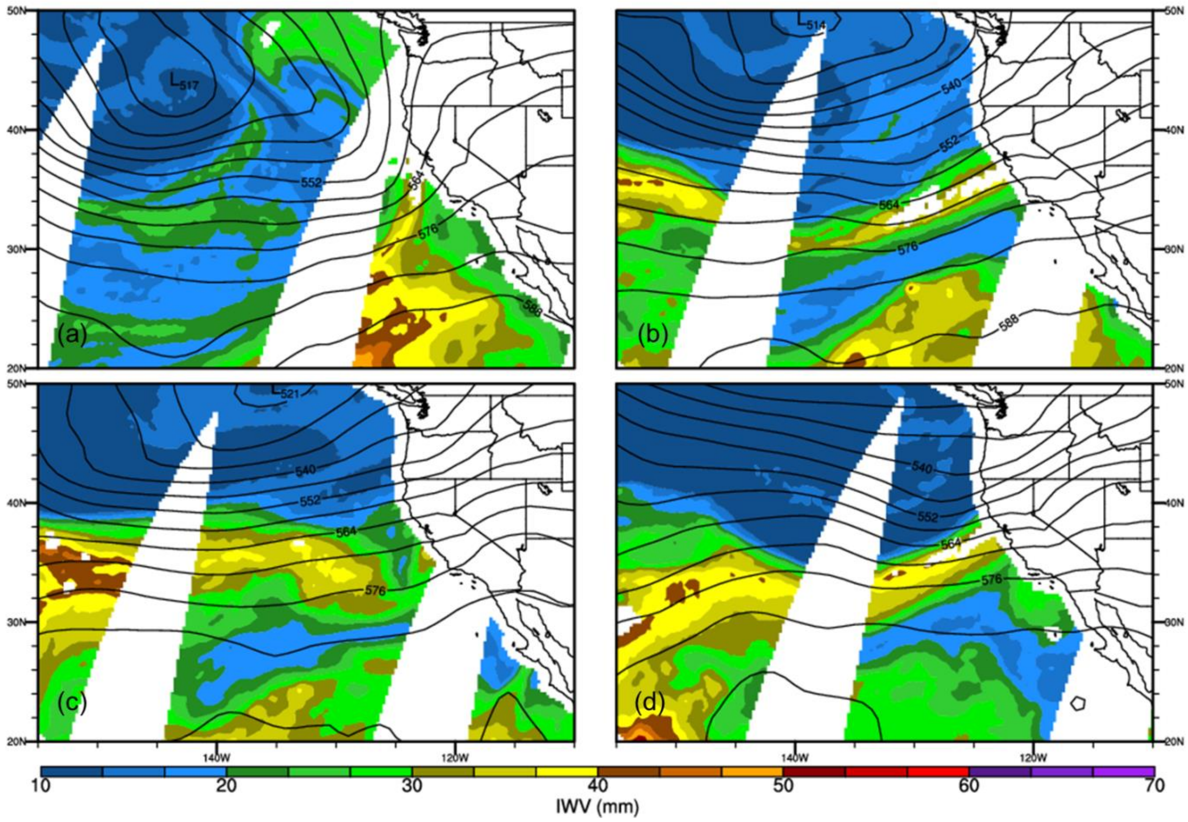

Figure 4: SSMIS IWV for AR Episodes 1-4 (a-d) overlaid with their most recent 500-hPa NARR height analysis: (a) Episode 1 (28 Nov): 1518 UTC SSMIS / 1500 UTC NARR; (b) Episode 2 (30 Nov): 1623 UTC SSMIS/ 1500 UTC NARR; (c) Episode 3 (01 Dec): 1441 UTC SSMIS / 1500 UTC NARR; and (d) Episode 4 (02 Dec): 1600 UTC SSMIS/ 1500 UTC.

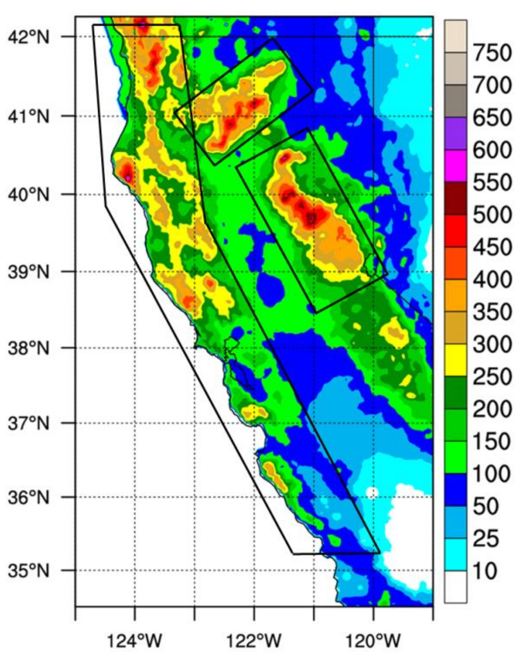

Figure 5: NCEP Stage IV accumulated rainfall (mm) from 0000 UTC 28 Nov through 1800 UTC 03 Dec 2012. The three polygons represent the three regions of maximum rainfall accumulations: Coastal Range Mountains (left), the Trinity Alps/ Mt. Shasta Region (top center), and the Northern Sierra Nevada (right).

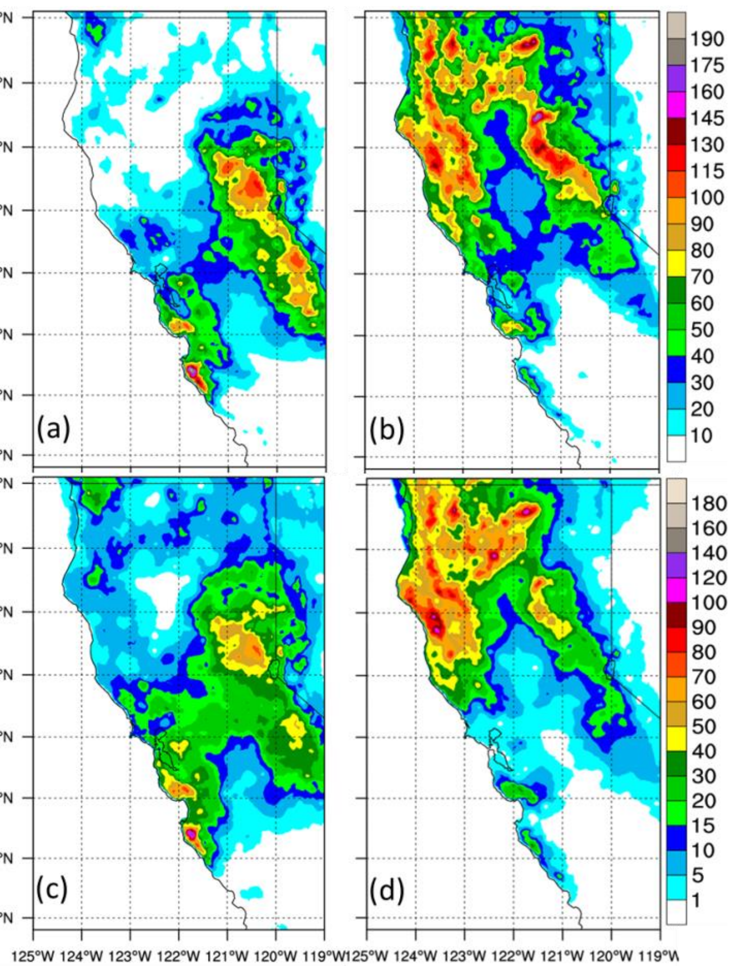

Figure 6: NCEP Stg. IV time periods with the maximum 12-hrly (a-b) and 6-hrly (c-d) rainfall accumulations (mm) for Episode 2 (a,c) and Episode 4 (b,d) from Table 2.

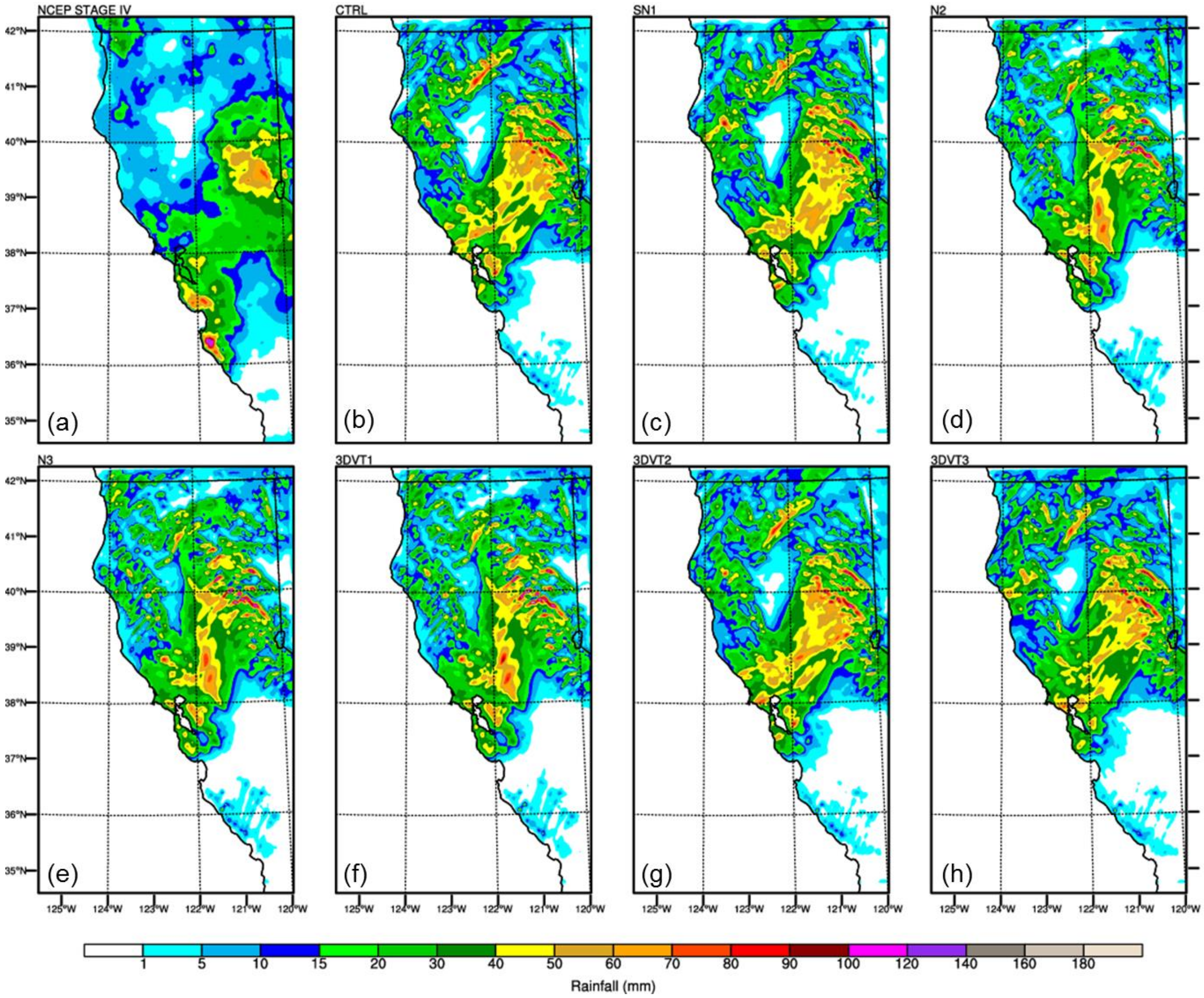

Figure 7: 6-hrly accumulated rainfall during Episode 2 (1200 - 1800 UTC 30th) in Domain 2 for (a) NCEP Stg. IV (b) CTRL (c) SN1 (d) N2 (e) N3 (f) 3DVT1 (g) 3DVT2 (h) 3DVT3

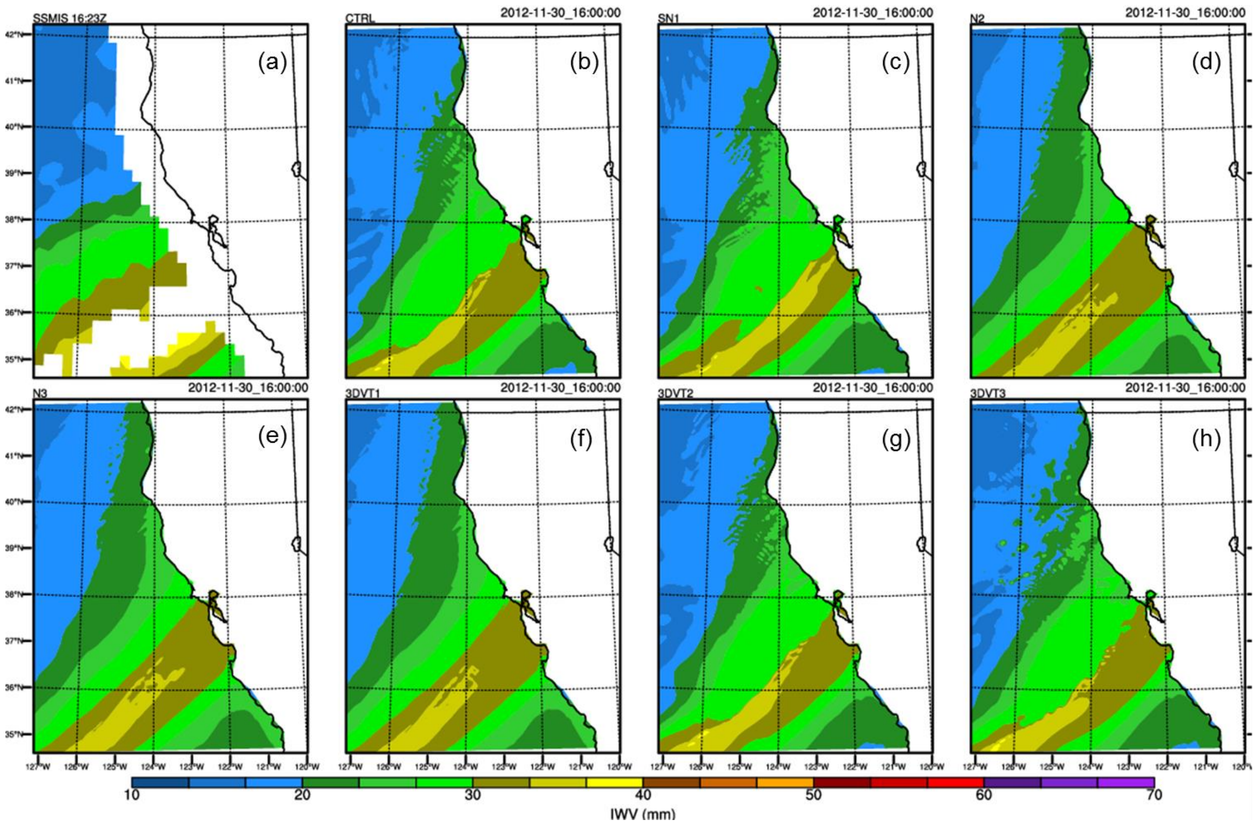

Figure 8: IWV in Domain 2 during Episode 2 on 30 Nov 2012 for (a) SSMIS at 1623 UTC and the WRF experiments (b-d) valid for 1600 UTC: (b) CTRL (c) SN1 (d) N2 (e) N3 (f) 3DVT1 (g) 3DVT2 (h) 3DVT3.

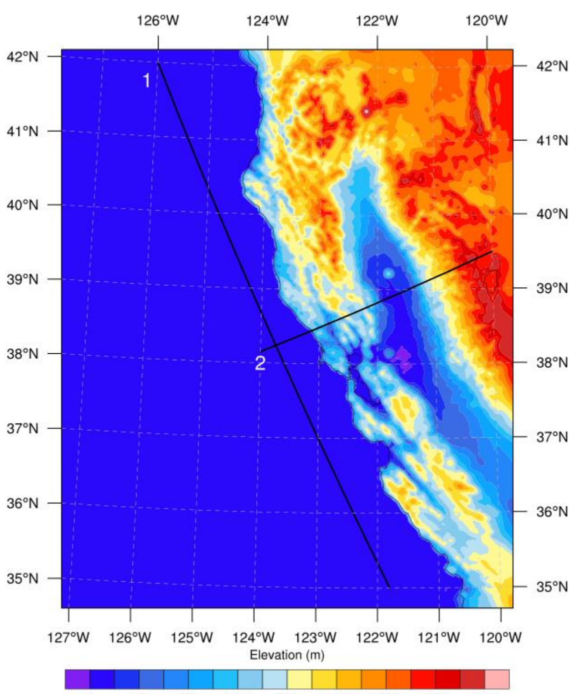

Figure 9: N-S along-coast cross-section (Line 1) and W-E cross-section through the Sacramento Valley (Line 2).

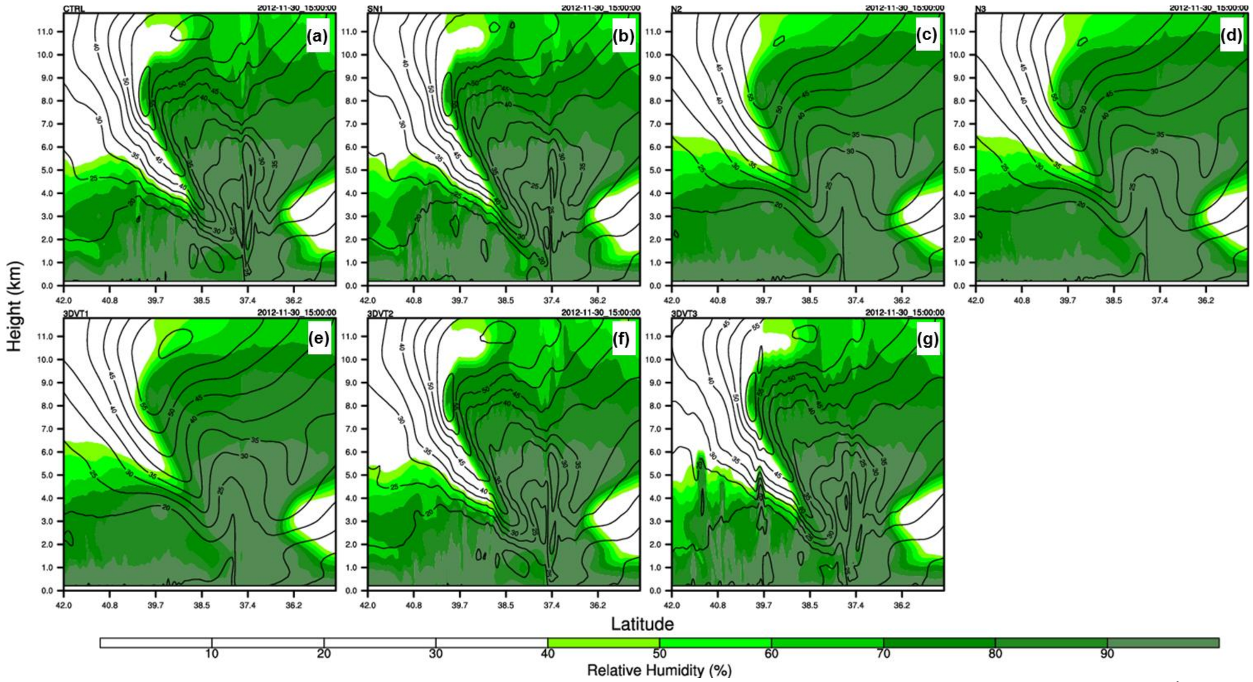

Figure 10: N-S along-coast cross section (Line 1) of relative humidity (shaded contours) and wind speed (m s^{-1}) (solid black contours) during Episode 2 at forecast hour 63 (1500 UTC 30^{th}) for each experiment: (a) CTRL (b) SN1 (c) N2 (d) N3 (e) 3DVT1 (f) 3DVT2 (g) 3DVT3.

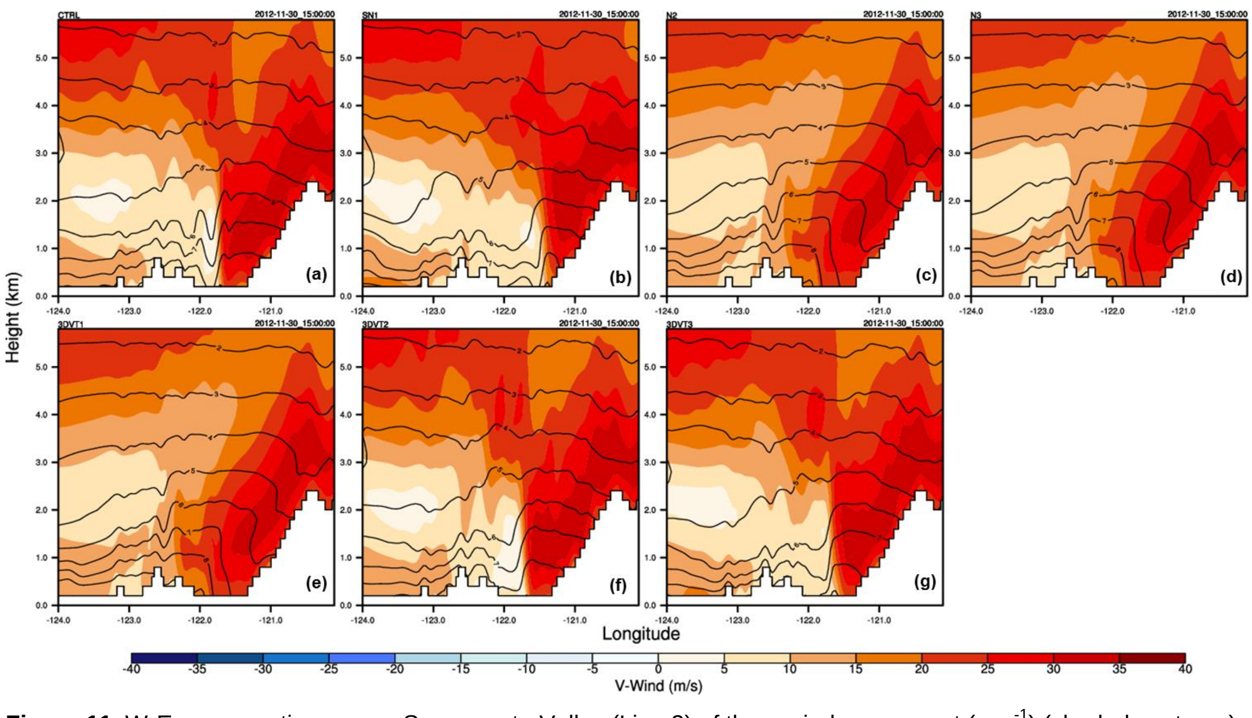

Figure 11: W-E cross section across Sacramento Valley (Line 2) of the v-wind component (m s^{-1}) (shaded contours) and specific humidity (g kg^{-1}) (solid contours) during Episode 2 at forecast hour 63 (1500 UTC 30^{th}) for each experiment: (a) CTRL (b) SN1 (c) N2 (d) N3 (e) 3DVT1 (f) 3DVT2 (g) 3DVT3.

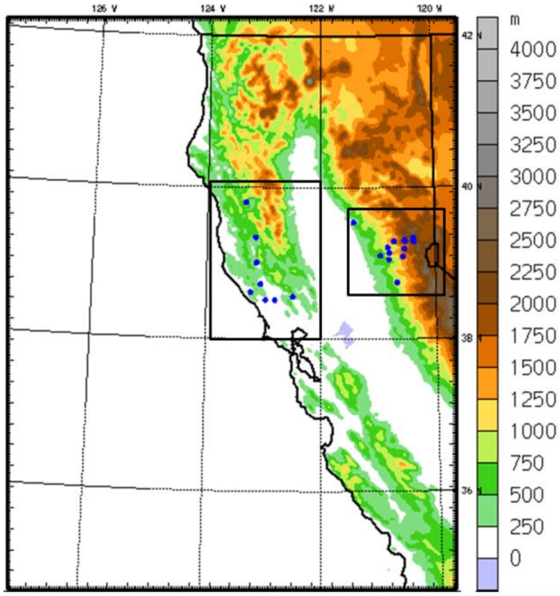

Figure 12: North Central Coastal Range (left box) and Windward Sierra Nevada (right box) for area-averaged HMT sites for entire event accumulated rainfall time series.

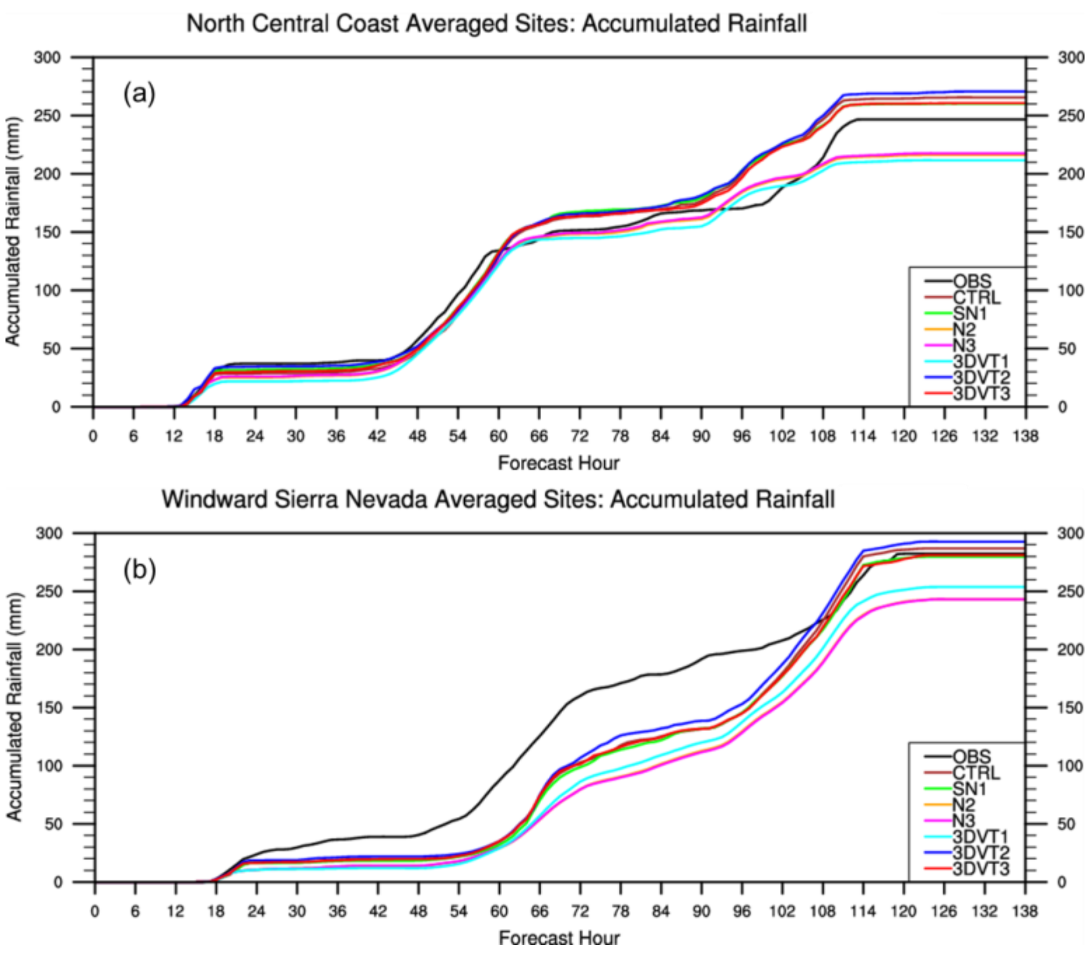

Figure 13: Area-averaged accumulated rainfall time series for (a) North Central Coast and (b) Windward Sierra Nevada HMT surface stations for observations (solid black) and WRF experiments.